Patterning of Wound-Induced Intercellular Ca2+ Flashes in a Developing Epithelium

Cody Narciso[1], **Qinfeng Wu**[1], **Pavel Brodskiy**[1], **George Garston**[2], **Ruth Baker**[2], **Alexander Fletcher**[2,#], and **Jeremiah Zartman**[1,#]

[1]Department of Chemical and Biomolecular Engineering, University of Notre Dame, 182 Fitzpatrick Hall, Notre Dame, IN 46556, USA

[2]Wolfson Centre for Mathematical Biology, Mathematical Institute, University of Oxford, Andrew Wiles Building, Radcliffe Observatory Quarter, Woodstock Road, Oxford, OX2 6GG, UK

Abstract

Differential mechanical force distributions are increasingly recognized to provide important feedback into the control of an organ's final size and shape. As a second messenger that integrates and relays mechanical information to the cell, calcium ions (Ca^{2+}) are a prime candidate for providing important information on both the overall mechanical state of the tissue and resulting behavior at the individual-cell level during development. Still, how the spatiotemporal properties of Ca^{2+} transients reflect the underlying mechanical characteristics of tissues is still poorly understood. Here we use an established model system of an epithelial tissue, the *Drosophila* wing imaginal disc, to investigate how tissue properties impact the propagation of Ca^{2+} transients induced by laser ablation. The resulting intercellular Ca^{2+} flash is found to be mediated by inositol 1,4,5-trisphosphate (IP_3) and depends on gap junction communication. Further, we find that intercellular Ca^{2+} transients show spatially nonuniform characteristics across the proximal-distal (PD) axis of the larval wing imaginal disc, which exhibit a gradient in cell size and anisotropy. A computational model of Ca^{2+} transients is employed to identify the principle factors explaining the spatiotemporal patterning dynamics of intercellular Ca^{2+} flashes. The relative Ca^{2+} flash anisotropy is principally explained by local cell shape anisotropy. Further, Ca^{2+} velocities are relatively uniform throughout the wing disc, irrespective of cell size or anisotropy. This can be explained by the opposing effects of cell diameter and cell elongation on intercellular Ca^{2+} propagation. Thus, intercellular Ca^{2+} transients follow lines of mechanical tension at velocities that are largely independent of tissue heterogeneity and reflect the mechanical state of the underlying tissue.

Keywords

#Correspondence: jzartman@nd.edu, alexander.fletcher@maths.ox.ac.uk.

1. INTRODUCTION

Calcium (Ca^{2+}) is a universal second messenger that integrates multiple signal inputs to coordinate downstream processes such as control of the cell cycle, apoptosis [1,2], cell migration [3], wound healing [4,5], gene expression [6] and differentiation state during development [7]. Although previous reports have highlighted the complex spatiotemporal dynamics in Ca^{2+} signaling in a variety of contexts, the information encoded in these dynamic responses remains largely undeciphered [3,8]. This is of particular importance in the case of developing epithelia, where it is increasingly recognized that biomechanical signaling, which is mediated in part by Ca^{2+} signaling [9–15], influences tissue morphogenesis and growth regulation [16–19].

An important first step towards understanding the role of Ca^{2+} signaling in organogenesis is to develop a more rigorous characterization of the dynamics of intercellular Ca^{2+} signaling. With the introduction and optimization of GCaMP6, a genetically encoded Ca^{2+} indicator (GECI), *Drosophila* has emerged as an important and genetically accessible model system to study Ca^{2+} signaling dynamics in epithelia [20–23]. After tissue wounding, a dramatic increase in cytoplasmic Ca^{2+} levels within cells surrounding the wound is observed [24–27]. In the *Drosophila* embryo, Ca^{2+} has been found to play a critical role in coordinating the wound inflammatory response through DUOX activation and subsequent release of hydrogen peroxide after wounding by laser ablation [26]. The rapid response (or 'flash') and decay of Ca^{2+} in the cells surrounding a wound correlates with waves of actomyosin and cell constriction that flow back towards the location of the wound's edge and later contribute to the formation of an actomyosin cable that drives wound closure [24]. Studies in the pupal thorax have shown that even cells that are several cell diameters away from a wound site are able to elongate in the direction of the wound to assist in wound closure [28]. Such observations highlight the importance of Ca^{2+} in the repair of damaged tissues and imply that Ca^{2+} may play a fundamental role in the relay of mechanical information to cells in the event of tissue damage as well as general changes in the mechanical environment. However, the scope of Ca^{2+} signaling in epithelial wound repair is still not fully understood, partly due to the largely qualitative level of analysis that has been done to date. In particular, the factors that govern the spatial extent and temporal patterning dynamics of Ca^{2+} signaling have not been elucidated.

Toward this end, we have performed a quantitative analysis of the transient intercellular Ca^{2+} flashes following localized laser ablation of cells in the pouch of the wing imaginal disc. The wing imaginal disc is a larval progenitor organ, consisting of two connected layers of epithelial cells that later develops into the adult wing and thorax (Fig. 1). The wing disc grows considerably during larval development, increasing from approximately 50 to 50,000 cells [29,30]. It consists of a simple and relatively flat epithelial cell sheet and has been intensively studied as a model for pattern formation and size control during epithelial organogenesis [18,31]. The larval wing disc also demonstrates extraordinary regenerative capacity and is able to fully repair and produce a correctly patterned adult wing after losing up to 50% of its cells [32], making it an important model system for studying regeneration. The wing disc also lends itself to *ex vivo* culture and live-imaging over the course of multiple hours [33] or more infrequently with *in vivo* imaging [34]. In particular, the oval-

shaped wing disc pouch, which is responsible for forming the adult wing blade, is located in the center of the wing disc and is ideal for examination of Ca^{2+} dynamics in epithelia due to its relative flatness and optical accessibility. The pouch is divided into well-defined developmental compartments separated by anterior-posterior (AP) and dorsal-ventral (DV) axes (Fig. 1A, B).

Similar to Ca^{2+} flashes in the embryo and pupal notum, we find that localized ablation in a *Drosophila* wing disc pouch induces a Ca^{2+} flash that propagates across multiple cell diameters [24,26]. Observations of Ca^{2+} flash dynamics from multiple discs reveal conserved qualitative features of the flash, in particular, the formation of spatially asymmetric elliptical profiles farther from the center of the pouch (Fig. 1C, D). To explain this spatial variation in asymmetry, we analyzed computational simulations of intercellular Ca^{2+} dynamics. From an examination of the previous literature and an initial pharmacological study in the wing disc, we chose a model based on the regulation of Ca^{2+} transport into the cytoplasm from endoplasmic reticulum (ER) stores, which is stimulated by the kinetics of IP_3. Stimulation by IP_3 is a conserved mechanism through which Ca^{2+} signals are transduced in many model tissues and has been used successfully in the past to recapitulate both qualitative and quantitative features of mechanically-induced Ca^{2+} flashes in computational models [8,35–37]. Here, we have quantified the dynamics of Ca^{2+} flashes in developing *Drosophila* wing discs, which exhibit both cell size and anisotropy gradients across the epithelium. Comparison between experimental and computational results supports the determination that the spatial asymmetry in Ca^{2+} propagation is principally explained by a gradient of cell shape anisotropy present across the proximal-distal axis of the disc. Although not a significant input to flash anisotropy, the gradient of apical cell area impacts the total flash area and velocity of the flash.

2. MATERIALS AND METHODS

2.1 Fly lines and genetics

The GCaMP6f Ca^{2+} sensor [20] was expressed ubiquitously in 3rd instar wing imaginal discs or constrained to the wing disc pouch using the GAL4-UAS system - *tub*-GAL4>UAS-*GCaMP6f* and *nub*-GAL4>UAS-*GCaMP6f,* respectively [38]. To visualize cell boundaries for the purpose of examining cell size distribution within the wing disc, discs from 3rd instar larvae of DE-Cadherin::GFP were used [39]. All flies were raised at 25 °C and 70% relative humidity on standard culture medium, and crosses were made using standard techniques [40].

2.2 Laser ablation experiments and Ca^{2+} visualization

Third instar wing imaginal discs from tub-GAL4>UAS-GCaMP6f larva were dissected and cultured in an *ex vivo* disc imaging chamber described previously [33]. Discs were cultured in Schneider's *Drosophila* media with 6.2 μg/mL insulin (Sigma Aldrich, Saint Louis, MO) and 0.5% (v/v) penicillin-streptomycin (Gibco (10,000 U/mL), Grand Island, NY). Imaging was performed on a Nikon Eclipse T*i* confocal microscope (Nikon Instruments Inc., Melville, NY) with a Yokogawa spinning disc and MicroPoint laser ablation system (Andor Technology, South Windsor, CT). Image data were collected on an iXonEM+ cooled CCD

camera (Andor Technology, South Windsor, CT) using MetaMorph® v7.7.9 software (Molecular Devices, Sunnyvale, CA). All experiments were performed immediately following dissection to minimize time in culture. Discs were imaged at a single z-plane, 40x magnification and 1-second intervals for a total period of five minutes. At five seconds into the time-lapse recording, a point ablation was performed by targeting the approximate center of a single cell in the pouch for 0.2 seconds to stimulate a Ca^{2+} response. The relative size and extent of a characteristic ablation is shown in Supplementary Material, Fig. S1. Multiple spatially separated ablations (up to nine) were performed on each cultured disc in order to capture dynamics across the full extent of the pouch. Each ablation occurred at a unique location in different regions to ensure that previous ablations did not interfere with the propagation of subsequent experiments. As the extent of the 3rd instar pouch is larger than the field of view at 40x magnification, multiple tiles were stitched together in post-processing to create a picture encompassing the entire disc pouch.

2.3 Pharmacological investigation of the Ca^{2+} flash response

Third instar wing imaginal discs were dissected as above in the media described with addition of either 2-ABP (IP_3 receptor – IP_3R) [41], thapsigargin (sarco/endoplasmic reticulum Ca^{2+}-ATPase - SERCA) [42], carbenoxolone (gap junctions) [43], dantrolene (ryanodine receptor - RyR) [44], ruthenium red (RyR) [45], or LY294002 (phosphoinositide 3-kinase - PI3K) [46]. Each of these was selected to inhibit the particular component of the Ca^{2+} pathway (in parenthesis). Discs were incubated in media with or without the selected compound for one hour before ablation and imaging (as above). Thapsigargin and dantrolene were obtained from Enzo Life Sciences (Farmingdale, NY); 2-APB, ruthenium red, and LY294002 were obtained from Tocris Bioscience (Bristol, UK); carbenoxolone was obtained from Sigma Aldrich (St. Louis, MO).

2.4 Image processing and analysis

Time-lapse videos of Ca^{2+} flashes were analyzed with the open-source software Fiji [47]. A projection of average pixel intensity with time was performed on each of these video stacks to provide an accurate picture of each flash centroid with landmark features from the pouch background and the resulting tiles manually stitched using the plugin MosaicJ [48]. The flashes in each stitched pouch were manually segmented by thresholding the stitched pouches using the 'Default' setting and added to the Region of Interest (ROI) manager using the 'Analyze Particles…' function. The entire pouch was manually outlined by an arbitrary n-sided polygon and the centroid of this polygon calculated to provide the pixel coordinates of the pouch center. An ellipse was also fit to this defined polygon to define the major and minor axes for the purposes of normalization. A custom Fiji macro was then applied to each flash ROI to provide relevant distance and slope measurements from the pouch centroid to the flash centroid.

To compensate for size variation between pouches, the absolute distance in x and y from the pouch centroid to the flash centroid was normalized by dividing by the length of the major axis of the best-fit ellipse for the pouch (Fig. 1A). For a quantitative description of flash asymmetry, the standard deviation projection for each flash was generated to provide a clear spatial outline of the flash with minimal background. These flashes were segmented using

the Yen autothresholding algorithm [49], which provided a robust and accurate segmentation in all cases observed. The segmented individual flashes were added to the ROI manager in Fiji and a second custom macro was run to calculate the fractional anisotropy of the flash, S. This quantity is defined in terms of the major and minor axes of the best-fit ellipse for each flash, denoted by λ_+ and λ_-, respectively, as follows [34],

$$S = \frac{|\lambda_+| - |\lambda_-|}{|\lambda_+| + |\lambda_-|} \quad (1)$$

Flashes were classed based on the normalized distance between the flash centroid and the pouch centroid, z, as being either central ($0.50 \geq z$) or peripheral ($0.50 < z$). MATLAB was used to generate a series of boxplots comparing the morphological and kinetic features of the flashes from each class. The analysis encompassed a total of 40 flashes from a sample of nine 3rd-instar wing discs. The Fiji macros and MATLAB code used in the above analysis are provided in the Supplementary Material.

2.5 Determination of cell size distribution

Third instar DE-Cadherin::GFP wing discs were fixed in 4% formaldehyde solution and imaged on the microscope system described above at 100X magnification with a z-stack interval of 0.5 μm. The entire pouch was imaged using a 6×6 grid of individual image tiles with 10% overlap at the boundaries. Individual grid tiles were stitched into a high-resolution, whole-pouch montage using Fiji [47]. Cell shapes in the wing disc pouch were segmented using Seedwater Segmenter [50]. A sample of 12,349 cells from three 3rd instar wing discs was used. ImageJ was used to define an ellipse fitting the segmented pouch and the ellipse cropped to remove cells in the field of view that lay outside the bounds of the pouch. Next, cells on the boundary of this ellipse that were cropped such that the entire cell was no longer visible were removed using the flood-fill tool in ImageJ. A custom MATLAB script (see Supplementary Material) was used to determine the centroid of the pouch, the individual cell centroids, the convex apical cell areas and major/minor axes for each cell. Cell data were then sorted by convex area and the upper and lower 2% of cells cropped from further analysis to remove additional errors in the segmentation mask, which typically lie at either extreme. Color-coded maps of cell size and fractional anisotropy across the disc were generated using MATLAB.

2.6 Mathematical model for intercellular Ca^{2+} signaling

A number of mathematical models describing different aspects of intracellular Ca^{2+} dynamics have been developed previously [51]. Here we focus on a two-dimensional model describing the dynamics of intracellular Ca^{2+} previously developed for epithelial cells (Fig. 2A). A central process in this model is the release of Ca^{2+} from the ER into the cytoplasm, which is regulated by channels sensitive to the messenger molecule IP$_3$. An injury or mechanical stress to a cell can trigger activation of IP$_3$ within the cell that, in turn, binds to IP$_3$R on the store membranes, opening ion channels and releasing Ca^{2+} into the cytoplasm [52]. IP$_3$-receptors are associated with Ca^{2+}-induced- Ca^{2+}-release (CICR): a process in

which the uptake of cytoplasmic Ca^{2+} by IP_3R induces a release of Ca^{2+} from the internal stores. In this way, CICR increases the cytoplasmic concentration of Ca^{2+} in the short term. There is also a continuous pumping of Ca^{2+} from the cytoplasm into the ER through the SERCA pump [53]. Cytoplasmic Ca^{2+} and IP_3 may also diffuse to neighboring cells through gap junctions, thus propagating the activation and causing a distinct flash within the tissue [24,54,55]. The presence of both IP_3 and IP_3R have already been confirmed in *Drosophila* in previous studies and linked to CICR and Ca^{2+} homeostasis in multiple *Drosophila* tissues [46,56–59]. Antibody stains for IP_3R have also previously demonstrated the presence of IP_3R in the wing imaginal disc [60]. In the present study we link IP_3 to a Ca^{2+} flash response in the wing disc using a pharmacological screen of major Ca^{2+} pathway components (see Supplementary Material, Table S1).

To provide a simple model description that can account for the Ca^{2+} flash geometry, a continuum description with no explicit definition of individual cells was used to model intercellular Ca^{2+} dynamics within the wing disc pouch. This avoids the introduction of interior boundary conditions at individual cell membranes within the spatial domain and greatly increases the computational tractability and domain size that can be simulated. Without an explicit definition of cells, quantities representing the magnitude of cell size and cell anisotropy can be imposed on the tissue domain and easily varied to rapidly test the effects of model parameters on patterning of the Ca^{2+} flash.

The model is dependent on a single intracellular pool of Ca^{2+} and IP_3. It consists of the following system of coupled ordinary and partial differential equations that describe how the concentrations of Ca^{2+} and IP_3 vary in time and space [35]. Approximating a region of the wing disc pouch by a two-dimensional square domain of length L in x and y, we have

$$\frac{\partial P}{\partial t} = D_P^{\text{intra}} \left(\frac{\partial^2 P}{\partial x^2} + \frac{\partial^2 P}{\partial y^2} \right) - \frac{V_P P k_P}{k_P + P} \quad (2)$$

$$\frac{\partial C}{\partial t} = D_C^{\text{intra}} \left(\frac{\partial^2 C}{\partial x^2} + \frac{\partial^2 C}{\partial y^2} \right) + J_{\text{flux}} - J_{\text{pump}} + J_{\text{leak}} \quad (3)$$

$$\frac{dh}{dt} = \frac{1}{\tau_h} \left(\frac{k_2^2}{k_2^2 + c^2} - h \right) \quad (4)$$

Here $P(x, y, t)$, $C(x, y, t)$ and $h(t)$ denote the concentration of IP_3, the concentration of Ca^{2+} and the fraction of IP_3 receptors that have not been inactivated by Ca^{2+} at time $t \geq 0$ and position $(x, y) \in [0, L] \times [0, L]$, respectively. The Ca^{2+} fluxes J_{flux}, J_{pump} and J_{leak} represent the processes described above and schematized in Fig. 2, A. We use the functional form of the Ca^{2+} fluxes proposed previously [35], namely

$$J_{\text{flux}} = k_{\text{flux}} \mu(P) h \left[b + \frac{(1-b)C}{k_1 + C} \right] \quad (5)$$

$$J_{\text{pump}} = \frac{\gamma C^2}{k_\gamma^2 + C^2} \quad (6)$$

$$J_{\text{leak}} = \beta \quad (7)$$

The function $\mu(P)$ models the activation of the IP$_3$ receptor by IP$_3$ and is chosen to take the form

$$\mu(P) = \frac{P}{k_\mu + P} \quad (8)$$

The form of $\mu(P)$ was chosen from a previously developed model [35] to match experimental observations that the flash intensity is highest at the point of stimulation and decreases with radial distance. All model parameters along with their interpretations and values are given in Table 1. We note that the effective intracellular diffusion coefficient of IP$_3$ given in Table 1 is far greater than that of Ca^{2+}, implying that IP$_3$ will diffuse through the cell much faster than Ca^{2+}. Although Ca^{2+} ions are much smaller than IP$_3$ molecules, the presence of Ca^{2+} buffers in the cytoplasm significantly slow down the intracellular diffusion of Ca^{2+}, while the cell's internal structures slow diffusion of both Ca^{2+} and IP$_3$ [61].

Equations (2) – (8) were originally derived for the intracellular dynamics of Ca^{2+} and IP$_3$ [35,36,62]. To describe their intercellular dynamics, we must incorporate the passage of these species through gap junctions into neighboring cells. Gap junctions at cell membranes severely slow down the rate at which both Ca^{2+} and IP$_3$ propagate throughout a tissue. We represent this in the model by using approximate expressions for the effective intercellular diffusion coefficient tensors D_C and D_P as shown in equations (9) and (10). These approximate expressions may be derived using homogenization techniques which rely on the assumption that the ratio of a typical cell diameter to the width of the tissue is small [8]. For the third instar larvae examined here, the wing disc pouch typically consists of several thousand individual cells on the order of 2–6 μm in diameter while the pouch itself is >100 μm in diameter. To investigate the error introduced by this assumption, we examined a 1D cell-based model and compared the simulation output to the continuum case and find that the introduced error is less than one cell diameter at maximal flash area. For our flashes, which propagate across approximately 10 cell diameters this error is <10% (see Supplementary Material, Fig. S2). For elongated cells (for which the fractional anisotropy, S, is non-zero), these approximate expressions are anisotropic as described below.

To obtain an approximate expression for each intercellular diffusion coefficient tensor, we assume that cells within our region of tissue may be approximated by rectangles aligned with the x and y axes, of length l and width jl. Without loss of generality we specify the aspect ratio, j, to take values in [0, 1]. We arrive at a closed-form expression for the effective intercellular diffusion coefficient tensor for Ca^{2+}, D_C, which is given by

$$D_C = \begin{pmatrix} D_C^x & 0 \\ 0 & D_C^y \end{pmatrix} = \begin{pmatrix} \left(1/D_C^{intra} + 1/l\alpha_C\right)^{-1} & 0 \\ 0 & \left(1/D_C^{intra} + 1/jl\alpha_C\right)^{-1} \end{pmatrix} \tag{9}$$

where D_C^{intra} is the intracellular diffusion coefficient of Ca^{2+} and a_C is the permeability of the cell membrane to Ca^{2+}. The expression for D_P takes a similar form. For further details on the use of homogenization theory to derive effective intercellular diffusion coefficients, see for example [8].

We assume each intracellular diffusion coefficient and permeability coefficient to be constant and spatially uniform. It is reasonable to assume an isotropic intracellular diffusion coefficient as this has been shown to recapitulate experimental observations in a number of model systems [8,36]. Since experimental mRNA evidence suggests that gap junctions are spatially uniform in the developing wing disc, it is assumed that the properties of the cell membrane can be approximated as homogenous [47]. Thus, we assume constant spatial permeability of cell membrane to both IP_3 and Ca^{2+} [54]. We further assume that membrane effects are the major source of anisotropy in any direction. We assume that the cell size l and aspect ratio j vary over length scales across the wing imaginal disc that are much larger than l, and thus that we may substitute these parameters with slowly varying functions of position in equation (9) in order to study the effect of variations in these quantities on the shape of the resulting Ca^{2+} flash.

For consistency of notation, we express the aspect ratio, j, in equation (9) in terms of the fractional anisotropy, $j = (1 - S)/(1+S)$, in the following. To close the model, we supplement equations (2)–(9) with zero-flux boundary conditions at each edge of the tissue ($x = 0$, $x = L$, $y = 0$, $y = L$). The laser ablation initial condition is modeled using an integrated IP_3 stimulus of 0.01 μM from $t = 0$ s to $t = 0.2$ s for a small 4 μm diameter circular element at the center of the domain. The IP_3 stimulus induces a Ca^{2+} flash event. IP_3 has been shown to stimulate a Ca^{2+} response in multiple cell types [26,37]. Further, it has been demonstrated previously that IP_3 will diffuse much faster than Ca^{2+} in a tissue within a range of physiological concentrations due to the presence of Ca^{2+} buffers in the cytoplasm [61]. This indicates that the observed Ca^{2+} flash is essentially a diffusive wave of IP_3 triggering Ca^{2+} release in adjoining cells rather than diffusion of Ca^{2+} from the initially stimulated cell. In the rest of the domain we impose a spatially uniform initial condition at $t = 0$, with P and h taking the values zero and one respectively. C takes its steady-state value according to equation (10).

We solve the model numerically using a simple explicit finite difference method with spatial step size $\Delta x = \Delta y = 0.5$ μm and time step $\Delta t = 0.001$ s, chosen small enough to ensure

numerical stability. A MATLAB implementation of this numerical scheme is provided in the Supplementary Material.

3. RESULTS AND DISCUSSION

3.1 Pharmacological characterization of laser induced Ca^{2+} flashes

To test the role of gap junctions in propagating the flash response, we incubated discs for 1 hour in 30 μM carbenoxolone, a widely used gap junction inhibiter [43]. Incubation of the disc with carbenoxolone (Cbx) resulted in dramatically reduced flash propagation when compared to controls (Fig. 2 B,C). This suggests that propagation of Ca^{2+} and IP$_3$ through gap junctions into neighboring cells is required for propagation of the induced flash. In order to determine the role of IP$_3$ mediated intracellular Ca^{2+} release in flash propagation, a series of compounds targeting IP$_3$R, PI3K and SERCA were tested. IP$_3$R interacts with IP$_3$ in order to initiate a release of Ca^{2+} from the intracellular stores in the ER [63]. IP$_3$R was targeted by incubation of the wing disc for 1 hour with 200 or 400 μM 2-aminoethoxydiphenylborane (2-APB), an inhibitor of IP$_3$-mediated Ca^{2+} release [41]. PI3K is involved in the production of IP$_3$ and was targeted by incubation for 1 hour with 300 μM LY294002 (LY), a known inhibitor of PI3K that has been demonstrated to dampen wave propagation during *Drosophila* oocyte activation [46]. We see a dramatic reduction in flash propagation when discs are incubated with LY294002 (Fig. 2 B,D) or 2-ABP (Fig. 2 B,E). Taken together, these results strongly suggest an active role for IP$_3$ mediated Ca^{2+} release in the formation and propagation of the flash response. SERCA is the primary path by which cytoplasmic Ca^{2+} is pumped back into the ER to maintain a proper cytoplasmic Ca^{2+} concentration. SERCA was targeted by incubation for 1 hour with 50 μM thapsigargin (Thap), a non-competitive inhibitor of SERCA [42,64]. After incubation with thapsigargin discs demonstrated highly elevated levels of cytoplasmic Ca^{+2} (Fig. 2 B, F) [65,66]. Thapsigargin did not have any noticeable impact on the extent of the Ca^{2+} transient. After treatment with thapsigargin, the Ca^{2+} response was noticeably dimmer in comparison to the background, consistent with reduced pumping of Ca^{2+}back into the ER. Surprisingly, this is contrary to flashes induced in the embryonic epidermis, which show marked flash reduction when treated with 1 μM thapsigargin [26]. However, these observations are consistent with results from our computational model, which show a marked increase in cytoplasmic Ca^{2+} for increases in k$_\gamma$ (increasing K$_m$ of the SERCA pump) and reductions in γ (maximum pumping rate for the SERCA pump). These parameters also show negligible effect on maximum flash area and are not expected to significantly alter flash the propagation (see Supplementary Material). In fact, the steady state concentration of Ca^{2+} for the model simulations is entirely dependent on these two parameters and β (constant cytoplasmic leak from the ER) and takes the form of equation (10).

$$C_{ss} = \sqrt{\frac{\beta k_\gamma{}^2}{\gamma - \beta}} \quad (10)$$

In order to ensure that flash propagation was not due to the actions of ryanodine, another small molecule responsible for Ca^{2+} release from intracellular stores, we incubated discs with two separate inhibitors of the ryanodine receptor (RyR) – dantrolene (Dan) and ruthenium red (RuR) [44,45]. Neither inhibitor had any noticeable impact on the extent of flash propagation (Supplementary Material, Fig. S3).

3.2 Spatiotemporal dynamics of wound-induced intercellular Ca^{2+} flashes

Laser ablation in the wing imaginal disc pouch creates a Ca^{2+} flash that propagates to adjacent cells followed by a recession from the maximal extent of the flash back toward the ablated cell (Fig. 3A and Fig. S1). This observation is similar to recent experiments performed in the *Drosophila* embryonic epidermis and pupal notum which note similar flash events [24,26]. Cells in the embryonic epidermis tend to elongate preferentially with mechanical forces during embryogenesis and it was observed, qualitatively, that the induced flashes tended to elongate preferentially in the direction of cell elongation [26,28]. This is consistent with our results. Similar to our results with carbenoxolone, Innexin-2 null alleles caused a dramatic reduction of flash propagation. However, it was noted in the embryonic epidermis that treatment with 1 μM thapsigargin drastically reduced the extent of the flash. We did not observe a reduction in flash response in the wing imaginal disc when treated with 50 μM thapsigargin and observed elevated levels of cytoplasmic calcium.

Several key features are well conserved across an experimental set of 40 flashes in nine imaginal discs. Notably, ablations performed near the pouch periphery form more asymmetric shapes (Fig. 3B), which are generally elliptical ($S_{mean} = 0.15 \pm 0.06$, $S_{max} = 0.30$), than ablations performed near the pouch center ($S_{mean} = 0.09 \pm 0.05$, $S_{max} = 0.21$), which tend to be more circular ($p = 0.002$, single-factor ANOVA). This tendency towards elongation was quantified using the fractional anisotropy of the flashes. Flashes were scored as being either 'central' ($N = 16$) or 'peripheral' ($N = 24$) based on their normalized distance from the pouch centroid, z.

Flashes were further characterized by detailed analysis of their temporal area profile (Fig. 3A). Each flash was plotted and characterized by three basic parameters: full width at half max area (time scale), slope at first half max area (areal expansion rate), and slope at last half max (areal recession rate). We notice a distinct shift in the rate of change of flash area during flash recession. This shift takes the form of a dramatic reduction in the slope of the area curve (Fig. 3A) that is well conserved in 36/40 flashes. Previous work has suggested that gap junctions are gated channels which close as a function of increasing Ca^{2+} concentration and pH to protect surrounding tissue from the toxic effects of these ions [67,68]. In general, our observed shift in dynamics occurs during the recession of the flash after maximum area has been achieved. Maximum area is also achieved early in the temporal profile due to rapid initial propagation. It is likely that this shift in dynamics is due to the results of this gating effect slowing the flow of Ca^{2+} through the gap junctions in the cell membrane as cytoplasmic Ca^{2+} concentration rises rapidly after perturbation. Although we observe a significant difference ($d = 1.3$, $p < 0.01$) between the areal propagation rate (r $= 30 \pm 20$ μm^2/s) and the areal recession rate (r $= 10 \pm 10$ μm^2/s) across the entire set of 40 flashes, we see no significant difference between these rates with respect to center versus

peripheral flashes (Fig. 3E, F). We also do not see any significant patterning of flash timescale across the tissue (Fig. 3D). Cohen's *d* is used as a metric of effect size for large data sets where significance testing by *p*-values becomes misleading [69]. Both the effect size and *p*-value, where appropriate, are reported for direct comparison.

3.2 Comparison of cell size and anisotropy variation in 3rd instar discs

As cell size has been recently shown to be non-constant within the wing imaginal disc [34,70], the observed flash asymmetries prompted us to look more carefully at the spatial variation of cell size and anisotropy within the pouch (Fig. 4). A sample of 12,349 cells from three, 3rd instar disc pouches were segmented and cell size information was extracted using a custom MATLAB script. This revealed, as expected, that there is a tendency for cells to be smaller at the center of the pouch and that apical cell area can vary by up to a factor of three across the pouch (Fig. 4A, C). Further, a plot of cell anisotropy (Fig. 4B, D) demonstrates a tendency for cells along the pouch boundary to be more elongated than center cells. As the sample sizes are so large, *p*-values show highly significant results between the two regions of the disc. A more rigorous indication of size effects with Cohen's *d* provides an indication of how strong the effects are for the two groups irrespective of sample size [69].

Experimental characterization of Ca^{2+} flash asymmetries suggests that spatial variations in these values are correlated with the observed spatial variations of both cell size and cell anisotropy in the pouch. Our analysis shows that flashes tend to develop asymmetrically in the periphery of the pouch in regions where cell size and anisotropy tend to be more variable and transition more abruptly (Fig. 4). A previous study has shown that internal mechanical forces generated during growth by proliferating cells in the wing imaginal disc play a key role in patterning cell sizes and shapes in the disc [70,71].

3.3 Computational analysis of cell geometry parameters on Ca^{2+} flash shape

As both cell size and cell shape anisotropy both vary across the PD axis, it is not immediately clear which parameter most significantly influences the observed spatiotemporal dynamics of the Ca^{2+} flashes. We used a computational model to investigate the impact of both cell size and anisotropy on the spatial spread of the flash, which allows us to vary each variable independently (*Methods*). This model reproduced the effect of ablating a single cell by an initial sustained increase in IP_3 in the ablated cell. IP_3 has been shown to stimulate a Ca^{2+} response in multiple cell types experimentally and computational models of IP_3 stimulated Ca^{2+} flashes have been shown to faithfully recapitulate experimentally observed Ca^{2+} data in other studies [8,35]. Further, it has been demonstrated previously that IP_3 will diffuse an order of magnitude faster than Ca^{2+} in a tissue within a range of physiological concentrations [61]. This dramatic difference in the diffusivity of Ca^{2+} and IP_3 is due to the presence of intracellular buffers which act to slow the movement of Ca^{2+} [61]. This suggests that the observed Ca^{2+} flash is essentially a diffusive wave of IP_3 triggering Ca^{2+} release in adjoining cells rather than diffusion of Ca^{2+} from the initially stimulated cell. A sensitivity analysis was performed in order to identify the model parameters most significant in influencing each experimentally measured variable, in addition to the maximum and background Ca^{2+} levels. Results of the sensitivity analysis are shown in the Supplementary Material. Maximum area and propagation rates were found to be most

sensitive to IP_3 degradation and intercellular permeability of IP_3. Only minor adjustment of parameter values were necessary to obtain an *in silico* flash spread and timescale consistent with our experimentally observed flashes as compared to the base model developed for airway epithelial cells [35]. The maximum pump rate for the SERCA pump (γ) was increased 10%, the intercellular permeability to IP_3 (a_P) was decreased 90%, and the concentration of IP_3 at half-maximal degradation rate (k_P) was decreased by 50% from the values reported in [35] to obtain a flash timescale and maximum area in agreement with experimental data. The Ca^{2+} flux for active IP_3 receptors (k_{flux}) was increased from 3 μM s^{-1}, to 8 μM s^{-1} to increase the maximum Ca^{2+} concentration (intensity) of the observed flash. The value of k_{flux} serves only as a concentration-scaling factor in the model and does not significantly affect other aspects of the simulated flash.

In our analysis, we considered four representative scenarios to investigate the source of the Ca^{2+} anisotropy in the periphery of the wing pouch. In case I, we modeled a tissue with uniform cell size and aspect ratio across the spatial domain by setting $l = 4$ μm and $S = 0$. The chosen cell size represents the average size within our chosen range of variation for subsequent cases ($2 - 6$ μm), which is consistent with the three-fold increase in cell size we observed experimentally across 3rd instar wing disc pouches. In case II, the cell size, l, is varied linearly across the disc in the x-direction from 2 μm to 6 μm, $l(x, y) = 2 + 4x/L$ for $(x, y) \in [0, L] \times [0, L]$, but we preserve cell isotropy ($S = 0$). This case, in which the resulting effective intercellular diffusion tensors are isotropic, examines whether cell size alone explains the observed asymmetry in the Ca^{2+} flashes. In case III, the cell size is held constant across the spatial domain ($l = 4$ μm) but the fractional anisotropy S is varied linearly from 0 to 0.7 in the x-direction to represent cells becoming increasingly elongated along one axis of the tissue: $S(x, y) = 0.7x/L$ for $(x, y) \in [0, L] \times [0, L]$. Again, this chosen range is consistent with the experimentally observed range for the 3rd instar wing discs shown in (Fig. 4A). This case, in which the resulting effective intercellular diffusion tensors are anisotropic, examines whether cell anisotropy alone is enough to describe the observed asymmetry in Ca^{2+} flashes. In the last scenario, case IV, we vary both cell size (as prescribed for the case II) and cell anisotropy (as prescribed for case III) across the spatial domain. Simulation results for these four cases are shown in (Fig. 4).

For the chosen parameter values, we find that cell size variation across the disc produces no significant asymmetry in flash dynamics when compared to the homogeneous tissue case (Fig 5C I, II). We also observe that cells of equal size can still produce an asymmetric flash if they are sufficiently elongated (Fig. 5C I, III) and that the incorporation of heterogeneity in cell sizes does not significantly affect the asymmetry of the flash in this case (Fig 5C IV). The results of our model simulations correlate well with the experimental observations summarized in (Fig. 4) for flashes. These results demonstrate that observed variance in cell size alone is not sufficient to pattern Ca^{2+} flashes and that it is instead the extent and the direction of elongation that work to pattern the spatial extent of the Ca^{2+} flash. We also tested the extreme case of instantaneous jumps in cell size and cell anisotropy by setting each half of the domain to the respective minimum and maximum values. Even for this extreme case, we find no appreciable elongation of the computational flash for abrupt changes in cell size (Supplementary Material, Fig. S4).

3.4 Computational analysis of cell geometry parameters on Ca^{2+} flash velocity and area

The model was also used to characterize the impact of cell size and cell anisotropy on the areal dynamics and maximum area of the flash. These results are summarized in Fig. 6. For these simulations, effective size differences, ΔL, and gradient of anisotropy, ΔS, represent linear variation across the computational domain starting at minimum value of 2 μm for cell size and 0 for fractional anisotropy. For simulations with a variable cell size, the imposed anisotropy is $S = 0$. For simulations with variable cell anisotropy, the imposed cell size is $L = 4$ μm. The model suggests a linear increase in maximum flash area with increasing effective cell size and a linear decrease with increasing effective cell anisotropy (Fig. 6A, B). The model also predicts a linear increase in flash timescale and areal expansion/recession with increasing cell size (Fig. 4C, D). A corresponding linear decrease in these variables is predicted for increasing cell anisotropy (Fig. 4E, F). The predicted opposing effects of cell size and cell anisotropy on maximum area and areal propagation/recession of the flash suggest an explanation for the experimentally observed homogeneity in flash area and areal propagation/recession of the flash throughout the pouch. As both cell size and cell elongation effectively increase across the PD axis of the pouch, the local anisotropy works to pattern the flash asymmetrically in space, but the corresponding gradient in cell size works to balance out impact on propagation, recession and area. Previous studies have also demonstrated that the velocity of long-distance Ca^{2+} transients are remarkably constant as they travel across both epithelial and endothelial cells [72]. Our model suggests that the opposing effects of cell size and cell anisotropy offer a possible mechanism through which wave speeds are conserved in a heterogeneous, anisotropic tissue, a feature that is likely a conserved in epithelial systems.

The model proposed here offers no description of Ca^{2+} concentration-dependent dynamics of gap junction permeability in the disc. Gap junctions assumed to have uniform permeability in time and space are sufficient to reproduce the experimentally observed flash elongation, maximum area, and full width at half maximum area. However, previous studies suggest that gap junctions actively close in response to high Ca^{2+} to shield neighboring cells from a toxic overdose [67,68]. Our experimental time-plots of area demonstrate a distinct shift in dynamics during flash recession that is suggestive of this drop in intercellular permeability. While the flash area increases quadratically during the initial phase of propagation, during recession, the flash follows higher-order polynomial dynamics. In contrast, the areal dynamics of our model demonstrate quadratic behavior throughout the entire simulation and we are unable to reproduce the differential propagation and recession velocities seen experimentally with our current phenomenological model. Ions other than Ca^{2+} have also been shown to reduce gap junction permeability [67,68,73]. Additionally, the exact nature of gap junction decoupling as a result of high Ca^{2+} concentration has only recently begun to be rigorously investigated [74]. Therefore, incorporation of the additional complexities introduced by Ca^{2+} dependent spatiotemporal regulation of gap junction permeability is a subject for future investigation.

4. CONCLUSIONS AND OUTLOOK

Previous studies have established the relationship between mechanical forces exerted by growth and cellular patterning in the tissue [16,75]. Recent evidence in both the wing imaginal disc and the developing embryo demonstrate that cell shape deformations correlate strongly with patterns of mechanical forces in the tissue [34,76]. These studies suggest that as the wing disc grows, cells in the center of the disc are subjected to compressive forces as the tissue expands outwards, while cells at the edge of the tissue are subjected to tensile forces [77,78]. These forces lead to the experimentally observed gradients in cell size and cell anisotropy.

Ca^{2+} signaling is instrumental in regulating many fundamental cellular processes from proliferation to wound healing [24]. Here we investigated the fast Ca^{2+} response after wounding in 3rd instar wing discs to explore how mechanical heterogeneity in a tissue impacts Ca^{2+} signaling. We have established the role of IP_3 in propagating the observed flash response in wing discs through a pharmacological examination of the major Ca^{2+} pathway components. Inhibition of IP_3R and PI3K resulted in greatly diminished flash response. Further, chemical inhibition of gap junctions also resulted in a lack of flash propagation. We have also quantified the difference in asymmetry between flashes occurring along the pouch periphery and flashes occurring near the pouch center. Peripheral flashes tend to elongate into elliptical shapes, following the local elongation of cells around the pouch periphery. By contrast, central flashes tend to assume a more circular profile. We have demonstrated a significant difference in the asymmetry of Ca^{2+} dynamics in each of these two categories. We further showed that these observed asymmetries are consistent both with gradients of cell fractional anisotropy and cell size measured in the tissue.

Computational simulations allow us to decouple effects of cell size and anisotropy on intercellular Ca^{2+} signaling dynamics. To analyze the potential roles of cell size and cell anisotropy as a driving force of these observed spatiotemporal dynamics for wound-induced Ca^{2+} flashes, we compared simulation results from a computational model of Ca^{2+} dynamics to experimental data. The high level of conservation of Ca^{2+} signaling in eukaryotic systems enabled us to apply a model previously developed for epithelial tissues in other systems [35] and extend this to the epithelial cells of the *Drosophila* wing imaginal disc pouch. We constructed a continuum description of the intercellular Ca^{2+} dynamics by introducing effective diffusion coefficients that depend on the cell length scale and anisotropy. To enable a simple derivation of effective diffusion coefficients, we assumed cells to be rectangular: this assumption has been shown to recapitulate experimental observations in past models of mechanically stimulated Ca^{2+} waves in airway epithelial cells [8,35]. With this model, we found that the experimentally observed variations in flash asymmetry cannot be explained solely by a physiologically observed gradient of cell size within the tissue. We found that this asymmetry is instead most likely the direct result of heterogeneities in cell fractional anisotropy (elongation) within the tissue.

Given the established connections between cell elongation and mechanical forces within tissues, our work suggests that the observed asymmetric flashes propagate preferentially along existing lines of force within anisotropic tissues [34,70,75]. This work also

demonstrates that different aspects of spatiotemporal dynamics of Ca^{2+} signaling (area, velocity, anisotropy) can be attributed to either cell size effects or cell anisotropy. We also have shown that the computational model can be used to make predictions about the spatiotemporal dynamics of the Ca^{2+} flashes within the patterned tissue, providing a guide for future studies incorporating the cellular responses to Ca^{2+} transients. Recent evidence demonstrating that Ca^{2+} signaling is correlated with waves of actomyosin recruited to the wound site in the minutes following damage suggests that these flashes may also serve to recruit subunits necessary for repair and instruct surrounding cells to elongate towards, and close, the wound [24,28]. The close coupling between cell geometry and Ca^{2+} signaling could also provide a mechanism for the transfer of information regarding cell and tissue shapes across epithelia for a given mechanical stimulus.

In related work outside the scope of this study, we observe more complicated Ca^{2+} transients in response to other stimulation modalities (manuscript in preparation). Recent studies have shown that many factors can contribute to the elongation of a cell or tissue [79] and completely decoupling these factors is a daunting challenge. It remains for future investigations whether *fat* and *daschous* mutants, which are important for P/D axis patterning, growth control, and cell polarity [80], may impact the pattern of Ca^{2+} flashes apart from general considerations of cellular morphometry. Microfluidic platforms might also be used to artificially alter cellular aspect ratio and observe changes to an induced Ca^{2+} response [81]. This work provides an important foundation for understanding how cell properties affect or encode information in intercellular Ca^{2+} responses. This can be expanded in the future to couple a spatiotemporal description of Ca^{2+} signaling with dynamic cell shape changes [82,83] during growth or under physical deformations to provide additional experimental evidence of the relationships uncovered in this current study.

Supplementary Material

Refer to Web version on PubMed Central for supplementary material.

Acknowledgments

References

1. Kahl CR, Means AR. Regulation of Cell Cycle Progression by Calcium/Calmodulin-Dependent Pathways. Endocr Rev. 2003; 24:719–36. [PubMed: 14671000]

2. Orrenius S, Zhivotovsky B, Nicotera P. Regulation of cell death: the calcium–apoptosis link. Nat Rev Mol Cell Biol. 2003; 4:552–65. [PubMed: 12838338]

3. Wei C, Wang X, Chen M, Ouyang K, Song L-S, Cheng H. Calcium flickers steer cell migration. Nature. 2009; 457:901–5. [PubMed: 19118385]

4. Berridge MJ, Lipp P, Bootman MD. The versatility and universality of calcium signalling. Nat Rev Mol Cell Biol. 2000; 1:11–21. [PubMed: 11413485]

5. Markova O, Lenne P-F. Calcium signaling in developing embryos: Focus on the regulation of cell shape changes and collective movements. Semin Cell Dev Biol. 2012; 23:298–307. [PubMed: 22414534]

6. Dolmetsch RE, Xu K, Lewis RS. Calcium oscillations increase the efficiency and specificity of gene expression. Nature. 1998; 392:933–6. [PubMed: 9582075]

7. Boyce ST, Ham RG. Calcium-Regulated Differentiation of Normal Human Epidermal Keratinocytes in Chemically Defined Clonal Culture and Serum-Free Serial Culture. J Invest Dermatol. 1983; 81:33s–40s. [PubMed: 6345690]

8. Keener, JP.; Sneyd, J. Mathematical Physiology: I: Cellular Physiology. Springer; 2009.

9. Ando J, Yamamoto K. Flow detection and calcium signalling in vascular endothelial cells. Cardiovasc Res. 2013; 99:260–8. [PubMed: 23572234]

10. Benavides Damm T, Egli M. Calcium's Role in Mechanotransduction during Muscle Development. Cell Physiol Biochem. 2014; 33:249–72. [PubMed: 24525559]

11. Jones, TJ.; Nauli, SM. Mechanosensory Calcium Signaling *Calcium Signaling*. In: Islam, MS., editor. Advances in Experimental Medicine and Biology. Springer; Netherlands: 2012. p. 1001-15.

12. Abu Khamidakh AE, Juuti-Uusitalo K, Larsson K, Skottman H, Hyttinen J. Intercellular Ca(2+) wave propagation in human retinal pigment epithelium cells induced by mechanical stimulation. Exp Eye Res. 2013; 108:129–39. [PubMed: 23352832]

13. Ohata H, Tanaka K, Maeyama N, Yamamoto M, Momose K. Visualization of elementary mechanosensitive Ca2+-influx events, Ca2+ spots, in bovine lens epithelial cells. J Physiol. 2001; 532:31–42. [PubMed: 11283223]

14. Olsen SM, Stover JD, Nagatomi J. Examining the Role of Mechanosensitive Ion Channels in Pressure Mechanotransduction in Rat Bladder Urothelial Cells. Ann Biomed Eng. 2011; 39:688–97. [PubMed: 21104316]

15. Resnick A. Use of optical tweezers to probe epithelial mechanosensation. J Biomed Opt. 2010; 15:015005–015005–8. [PubMed: 20210445]

16. Aegerter-Wilmsen T, Smith AC, Christen AJ, Aegerter CM, Hafen E, Basler K. Exploring the effects of mechanical feedback on epithelial topology. Development. 2010; 137:499–506. [PubMed: 20081194]

17. Baena-Lopez LA, Nojima H, Vincent J-P. Integration of morphogen signalling within the growth regulatory network. Curr Opin Cell Biol. 2012; 24:166–72. [PubMed: 22257639]

18. Buchmann A, Alber M, Zartman JJ. Sizing it up: The mechanical feedback hypothesis of organ growth regulation. Semin Cell Dev Biol. 2014; 35C:73–81. [PubMed: 25020200]

19. Shraiman BI. Mechanical feedback as a possible regulator of tissue growth. Proc Natl Acad Sci U S A. 2005; 102:3318–23. [PubMed: 15728365]

20. Chen T-W, Wardill TJ, Sun Y, Pulver SR, Renninger SL, Baohan A, Schreiter ER, Kerr RA, Orger MB, Jayaraman V, Looger LL, Svoboda K, Kim DS. Ultrasensitive fluorescent proteins for imaging neuronal activity. Nature. 2013; 499:295–300. [PubMed: 23868258]

21. Nakai J, Ohkura M, Imoto K. A high signal-to-noise Ca2+ probe composed of a single green fluorescent protein. Nat Biotechnol. 2001; 19:137–41. [PubMed: 11175727]

22. Pastrana E. Sensors and probes: Calcium sensors reach new heights. Nat Methods. 2013; 10:824–824. [PubMed: 24143827]

23. Tian L, Hires SA, Mao T, Huber D, Chiappe ME, Chalasani SH, Petreanu L, Akerboom J, McKinney SA, Schreiter ER, Bargmann CI, Jayaraman V, Svoboda K, Looger LL. Imaging neural activity in worms, flies and mice with improved GCaMP calcium indicators. Nat Methods. 2009; 6:875–81. [PubMed: 19898485]

24. Antunes M, Pereira T, Cordeiro JV, Almeida L, Jacinto A. Coordinated waves of actomyosin flow and apical cell constriction immediately after wounding. J Cell Biol. 2013; 202:365–79. [PubMed: 23878279]

25. Clapham DE. Calcium signaling. Cell. 2007; 131:1047–58. [PubMed: 18083096]

26. Razzell W, Evans IR, Martin P, Wood W. Calcium Flashes Orchestrate the Wound Inflammatory Response through DUOX Activation and Hydrogen Peroxide Release. Curr Biol. 2013; 23:424–9. [PubMed: 23394834]

27. Wood W. Wound Healing: Calcium Flashes Illuminate Early Events. Curr Biol. 2012; 22:R14–6. [PubMed: 22240471]

28. Razzell W, Wood W, Martin P. Recapitulation of morphogenetic cell shape changes enables wound re-epithelialisation. Development. 2014:dev.107045.

29. Fain MJ, Stevens B. Alterations in the cell cycle of Drosophila imaginal disc cells precede metamorphosis. Dev Biol. 1982; 92:247–58. [PubMed: 6809511]

30. Garcia-Bellido A, Merriam JR. Parameters of the wing imaginal disc development of Drosophila melanogaster. Dev Biol. 1971; 24:61–87. [PubMed: 5001010]

31. Restrepo S, Zartman JJ, Basler K. Coordination of patterning and growth by the morphogen DPP. Curr Biol CB. 2014; 24:R245–55. [PubMed: 24650915]

32. Haynie JL, Bryant PJ. The effects of X-rays on the proliferation dynamics of cells in the imaginal wing disc ofDrosophila melanogaster. Wilhelm Rouxs Arch Dev Biol. 1977; 183:85–100.

33. Zartman J, Restrepo S, Basler K. A high-throughput template for optimizing Drosophila organ culture with response-surface methods. Dev Camb Engl. 2013; 140:667–74.

34. Heemskerk I, Lecuit T, LeGoff L. Dynamic clonal analysis based on chronic in vivo imaging allows multiscale quantification of growth in the Drosophila wing disc. Dev Camb Engl. 2014; 141:2339–48.

35. Sneyd J, Wetton BT, Charles AC, Sanderson MJ. Intercellular calcium waves mediated by diffusion of inositol trisphosphate: a two-dimensional model. Am J Physiol. 1995; 268:C1537–45. [PubMed: 7611375]

36. Höfer T, Venance L, Giaume C. Control and Plasticity of Intercellular Calcium Waves in Astrocytes: A Modeling Approach. J Neurosci. 2002; 22:4850–9. [PubMed: 12077182]

37. Long J, Junkin M, Wong PK, Hoying J, Deymier P. Calcium wave propagation in networks of endothelial cells: model-based theoretical and experimental study. PLoS Comput Biol. 2012; 8:e1002847. [PubMed: 23300426]

38. Duffy JB. GAL4 system in drosophila: A fly geneticist's swiss army knife. genesis. 2002; 34:1–15. [PubMed: 12324939]

39. Huang J, Zhou W, Dong W, Watson AM, Hong Y. Directed, efficient, and versatile modifications of the Drosophila genome by genomic engineering. Proc Natl Acad Sci. 2009 pnas.0900641106.

40. Ashburner, M. Drosophila: A laboratory handbook. Cold Spring Harbor Laboratory; 1989.

41. Xiao J, Liang D, Zhao H, Liu Y, Zhang H, Lu X, Liu Y, Li J, Peng L, Chen Y-H. 2-Aminoethoxydiphenyl borate, a inositol 1,4,5-triphosphate receptor inhibitor, prevents atrial fibrillation. Exp Biol Med Maywood NJ. 2010; 235:862–8.

42. Michelangeli F, East JM. A diversity of SERCA Ca2+ pump inhibitors. Biochem Soc Trans. 2011; 39:789–97. [PubMed: 21599650]

43. Diao H, Xiao S, Howerth EW, Zhao F, Li R, Ard MB, Ye X. Broad gap junction blocker carbenoxolone disrupts uterine preparation for embryo implantation in mice. Biol Reprod. 2013; 89:31. [PubMed: 23843229]

44. Zhao F, Li P, Chen SR, Louis CF, Fruen BR. Dantrolene inhibition of ryanodine receptor Ca2+ release channels. Molecular mechanism and isoform selectivity. J Biol Chem. 2001; 276:13810–6. [PubMed: 11278295]

45. Ma J. Block by ruthenium red of the ryanodine-activated calcium release channel of skeletal muscle. J Gen Physiol. 1993; 102:1031–56. [PubMed: 7510773]

46. Kaneuchi T, Sartain CV, Takeo S, Horner VL, Buehner NA, Aigaki T, Wolfner MF. Calcium waves occur as Drosophila oocytes activate. Proc Natl Acad Sci. 2015; 112:791–6. [PubMed: 25564670]

47. Schindelin J, Arganda-Carreras I, Frise E, Kaynig V, Longair M, Pietzsch T, Preibisch S, Rueden C, Saalfeld S, Schmid B, Tinevez J-Y, White DJ, Hartenstein V, Eliceiri K, Tomancak P, Cardona A. Fiji: an open-source platform for biological-image analysis. Nat Methods. 2012; 9:676–82. [PubMed: 22743772]

48. Thévenaz P, Unser M. User-friendly semiautomated assembly of accurate image mosaics in microscopy. Microsc Res Tech. 2007; 70:135–46. [PubMed: 17133410]

49. Sezgin M, Sankur B. Survey over image thresholding techniques and quantitative performance evaluation. J Electron Imaging. 2004; 13:146–68.

50. Mashburn DN, Lynch HE, Ma X, Hutson MS. Enabling user-guided segmentation and tracking of surface-labeled cells in time-lapse image sets of living tissues. Cytometry A. 2012; 81A:409–18. [PubMed: 22411907]

51. Falcke M. Reading the patterns in living cells —the physics of ca^{2+} signaling. Adv Phys. 2004; 53:255–440.

52. Goldbeter A, Dupont G, Berridge MJ. Minimal model for signal-induced Ca2+ oscillations and for their frequency encoding through protein phosphorylation. Proc Natl Acad Sci. 1990; 87:1461–5. [PubMed: 2304911]

53. MacLennan DH, Rice WJ, Green NM. The Mechanism of Ca2+ Transport by Sarco(Endo)plasmic Reticulum Ca2+-ATPases. J Biol Chem. 1997; 272:28815–8. [PubMed: 9360942]

54. Stebbings LA, Todman MG, Phillips R, Greer CE, Tam J, Phelan P, Jacobs K, Bacon JP, Davies JA. Gap junctions in Drosophila: developmental expression of the entire innexin gene family. Mech Dev. 2002; 113:197–205. [PubMed: 11960713]

55. Weir MP, Lo CW. Gap-junctional communication compartments in the Drosophila wing imaginal disk. Dev Biol. 1984; 102:130–46. [PubMed: 6698301]

56. Parry H, McDougall A, Whitaker M. Microdomains bounded by endoplasmic reticulum segregate cell cycle calcium transients in syncytial Drosophila embryos. J Cell Biol. 2005; 171:47–59. [PubMed: 16216922]

57. Agrawal N, Venkiteswaran G, Sadaf S, Padmanabhan N, Banerjee S, Hasan G. Inositol 1,4,5-Trisphosphate Receptor and dSTIM Function in Drosophila Insulin-Producing Neurons Regulates Systemic Intracellular Calcium Homeostasis and Flight. J Neurosci. 2010; 30:1301–13. [PubMed: 20107057]

58. Banerjee S, Joshi R, Venkiteswaran G, Agrawal N, Srikanth S, Alam F, Hasan G. Compensation of Inositol 1,4,5-Trisphosphate Receptor Function by Altering Sarco-Endoplasmic Reticulum Calcium ATPase Activity in the Drosophila Flight Circuit. J Neurosci. 2006; 26:8278–88. [PubMed: 16899722]

59. York-Andersen AH, Parton RM, Bi CJ, Bromley CL, Davis I, Weil TT. A single and rapid calcium wave at egg activation in Drosophila. Biol Open. 2015 BIO201411296.

60. Raghu P, Hasan G. The Inositol 1,4,5-Triphosphate Receptor Expression in Drosophila Suggests a Role for IP3 Signalling in Muscle Development and Adult Chemosensory Functions. Dev Biol. 1995; 171:564–77. [PubMed: 7556937]

61. Allbritton NL, Meyer T, Stryer L. Range of messenger action of calcium ion and inositol 1,4,5-trisphosphate. Science. 1992; 258:1812–5. [PubMed: 1465619]

62. Sneyd J, Charles AC, Sanderson MJ. A model for the propagation of intercellular calcium waves. Am J Physiol. 1994; 266:C293–302. [PubMed: 8304425]

63. Taylor CW, Tovey SC. IP3 Receptors: Toward Understanding Their Activation. Cold Spring Harb Perspect Biol. 2010; 2:a004010. [PubMed: 20980441]

64. Watson WD, Facchina SL, Grimaldi M, Verma A. Sarco-endoplasmic reticulum Ca2+ ATPase (SERCA) inhibitors identify a novel calcium pool in the central nervous system. J Neurochem. 2003; 87:30–43. [PubMed: 12969250]

65. Pierce WG, Zanette C, Caplice NM, Mackrill JJ. Calcium signalling in adult endothelial outgrowth cells. Biochem Biophys Res Commun. 2012; 417:358–63. [PubMed: 22155247]

66. Nath S, Goodwin J, Engelborghs Y, Pountney DL. Raised calcium promotes α-synuclein aggregate formation. Mol Cell Neurosci. 2011; 46:516–26. [PubMed: 21145971]

67. Peracchia C. Chemical gating of gap junction channels: Roles of calcium, pH and calmodulin. Biochim Biophys Acta BBA - Biomembr. 2004; 1662:61–80.

68. Berg, JM.; Tymoczko, JL.; Stryer, L. Biochemistry. W. H. Freeman; 2010.

69. Lin M, Lucas HC, Shmueli G. Research Commentary—Too Big to Fail: Large Samples and the p-Value Problem. Inf Syst Res. 2013; 24:906–17.

70. Mao Y, Tournier AL, Hoppe A, Kester L, Thompson BJ, Tapon N. Differential proliferation rates generate patterns of mechanical tension that orient tissue growth. EMBO J. 2013; 32:2790–803. [PubMed: 24022370]

71. Legoff L, Rouault H, Lecuit T. A global pattern of mechanical stress polarizes cell divisions and cell shape in the growing Drosophila wing disc. Dev Camb Engl. 2013; 140:4051–9.

72. Jaffe LF. The propagation speeds of calcium action potentials are remarkably invariant. Biol Cell Auspices Eur Cell Biol Organ. 2003; 95:343–55.

73. Shaw RM, Rudy Y. Ionic Mechanisms of Propagation in Cardiac Tissue Roles of the Sodium and L-type Calcium Currents During Reduced Excitability and Decreased Gap Junction Coupling. Circ Res. 1997; 81:727–41. [PubMed: 9351447]

74. Allen MJ, Gemel J, Beyer EC, Lal R. Atomic Force Microscopy of Connexin40 Gap Junction Hemichannels Reveals Calcium-dependent Three-dimensional Molecular Topography and Open-Closed Conformations of Both the Extracellular and Cytoplasmic Faces. J Biol Chem. 2011; 286:22139–46. [PubMed: 21543330]

75. Li Y, Naveed H, Kachalo S, Xu LX, Liang J. Mechanisms of Regulating Cell Topology in Proliferating Epithelia: Impact of Division Plane, Mechanical Forces, and Cell Memory. PLoS ONE. 2012; 7:e43108. [PubMed: 22912800]

76. Lynch HE, Veldhuis J, Brodland GW, Hutson MS. Modeling cell elongation during germ band retraction: cell autonomy versus applied anisotropic stress. New J Phys. 2014; 16:055003.

77. Schluck T, Aegerter CM. Photo-elastic properties of the wing imaginal disc of Drosophila. Eur Phys J E Soft Matter. 2010; 33:111–5. [PubMed: 20563622]

78. Nienhaus U, Aegerter-Wilmsen T, Aegerter CM. Determination of mechanical stress distribution in Drosophila wing discs using photoelasticity. Mech Dev. 2009; 126:942–9. [PubMed: 19748573]

79. Li Y, Naveed H, Kachalo S, Xu LX, Liang J. Mechanisms of Regulating Tissue Elongation in Drosophila Wing: Impact of Oriented Cell Divisions, Oriented Mechanical Forces, and Reduced Cell Size. PLoS ONE. 2014; 9:e86725. [PubMed: 24504016]

80. Matakatsu H, Blair SS. Interactions between Fat and Dachsous and the regulation of planar cell polarity in the Drosophila wing. Development. 2004; 131:3785–94. [PubMed: 15240556]

81. Kim D-H, Wong PK, Park J, Levchenko A, Sun Y. Microengineered Platforms for Cell Mechanobiology. Annu Rev Biomed Eng. 2009; 11:203–33. [PubMed: 19400708]

82. Fletcher AG, Osterfield M, Baker RE, Shvartsman SY. Vertex models of epithelial morphogenesis. Biophys J. 2014; 106:2291–304. [PubMed: 24896108]

83. Smith AM, Baker RE, Kay D, Maini PK. Incorporating chemical signalling factors into cell-based models of growing epithelial tissues. J Math Biol. 2012; 65:441–63. [PubMed: 21898111]

84. El-Kholy W, Macdonald PE, Lin J-H, Wang J, Fox JM, Light PE, Wang Q, Tsushima RG, Wheeler MB. The phosphatidylinositol 3-kinase inhibitor LY294002 potently blocks K(V) currents via a direct mechanism. FASEB J Off Publ Fed Am Soc Exp Biol. 2003; 17:720–2.

85. Parys B, Côté A, Gallo V, De Koninck P, Sík A. Intercellular calcium signaling between astrocytes and oligodendrocytes via gap junctions in culture. Neuroscience. 2010; 167:1032–43. [PubMed: 20211698]
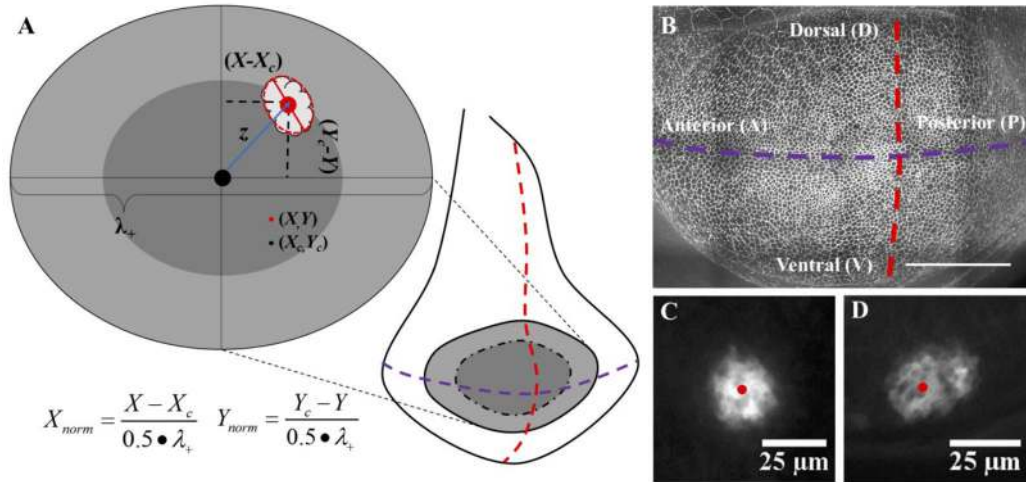
$$X_{norm} = \frac{X - X_c}{0.5 \bullet \lambda_+} \quad Y_{norm} = \frac{Y_c - Y}{0.5 \bullet \lambda_+}$$

FIGURE 1.

The *Drosophila* wing imaginal disc represents a versatile system for the study of wound-induced Ca^{2+} flashes. The wing disc is a relatively simple tissue, which exhibits extraordinary wound healing capacity. (**A**) Schematic of a full wing disc with the pouch shown in grey. The major developmental axes, the anterior-posterior (AP) (red) and dorsal-ventral (DV) (purple) are also shown. Flashes were classed based on the normalized distance between the flash centroid and the pouch centroid, z, as being either central ($0.50 \geq z$) or peripheral ($0.50 < z$). (**B**) Confocal image of a typical 3rd instar wing disc pouch. Here, cell boundaries are visualized with fluorescently-tagged E-Cadherin, DECad::GFP. The scale bar is 50μm. (**C**) Characteristic Ca^{2+} flash occurring near the pouch center (z=0.2). (**D**) Characteristic flash situated near to the pouch periphery (z=0.9). In **C** and **D**, red dots mark the ablation target.
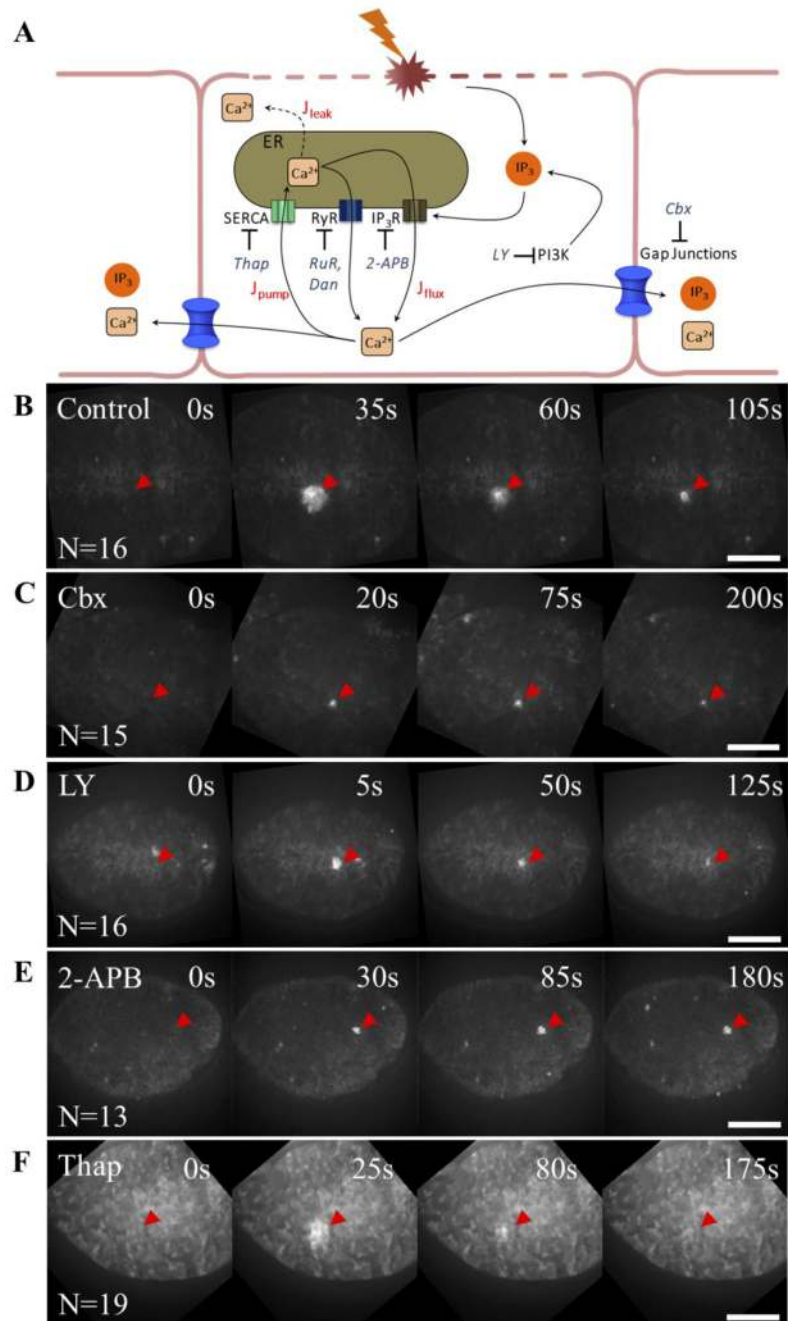
FIGURE 2.
(**A**) Schematic of the model of intracellular Ca^{2+} dynamics in response to wounding, driven by the triggering of inositol 1,4,5-trisphosphate (IP_3) dependent release of internal Ca^{2+} stores from the endoplasmic reticulum (ER) through activation of the IP_3 receptor (IP_3R). Cytoplasmic IP_3 then diffuses to neighboring cells through gap junctions, inducing a similar response, thus propagating a Ca^{2+} flash across several cells at the wounding site. Ca^{2+} in the cytoplasm is also continuously pumped back into the ER by the sarco/endoplasmic reticulum Ca^{2+}-ATPase (SERCA) pump. A slow leak of Ca^{2+} through the ER membrane

(J_{leak}) also adds to cytoplasmic Ca^{2+}. Figure adapted from [35]. Pharmacological targeting of relevant Ca^{2+} pathway components shown by negative inhibition arrows. Thapsigargin (Thap) inhibits SERCA, ruthenium red (RuR) and dantrolene (Dan) inhibit RyR, 2-APB inhibits IP_3R, LY294002 (LY) inhibits PI3K (IP_3 production) and carbenoxolone (Cbx) inhibits gap junctions. (**B**) Representative Ca^{2+} flash under normal culture conditions. (**C**) Ablation in tissue incubated for one hour with 30 μM carbenoxolone shows severely limited propagation of the Ca^{2+} transients. (**D**) Ablation in tissue incubated for one hour with 300 μM LY294002 shows severely limited propagation of the Ca^{2+} transients when IP_3 production is inhibited. (**E**) Ablation in tissue incubated for one hour with 400 μM 2-APB shows severely limited propagation of the Ca^{2+} transients. (**F**) Ablation in tissue incubated for one hour with 50 μM thapsigargin shows elevated levels of cytoplasmic Ca^{2+} consistent with deactivation of the SERCA pump and reduced flash propagation. All scale bars are 50 μm.
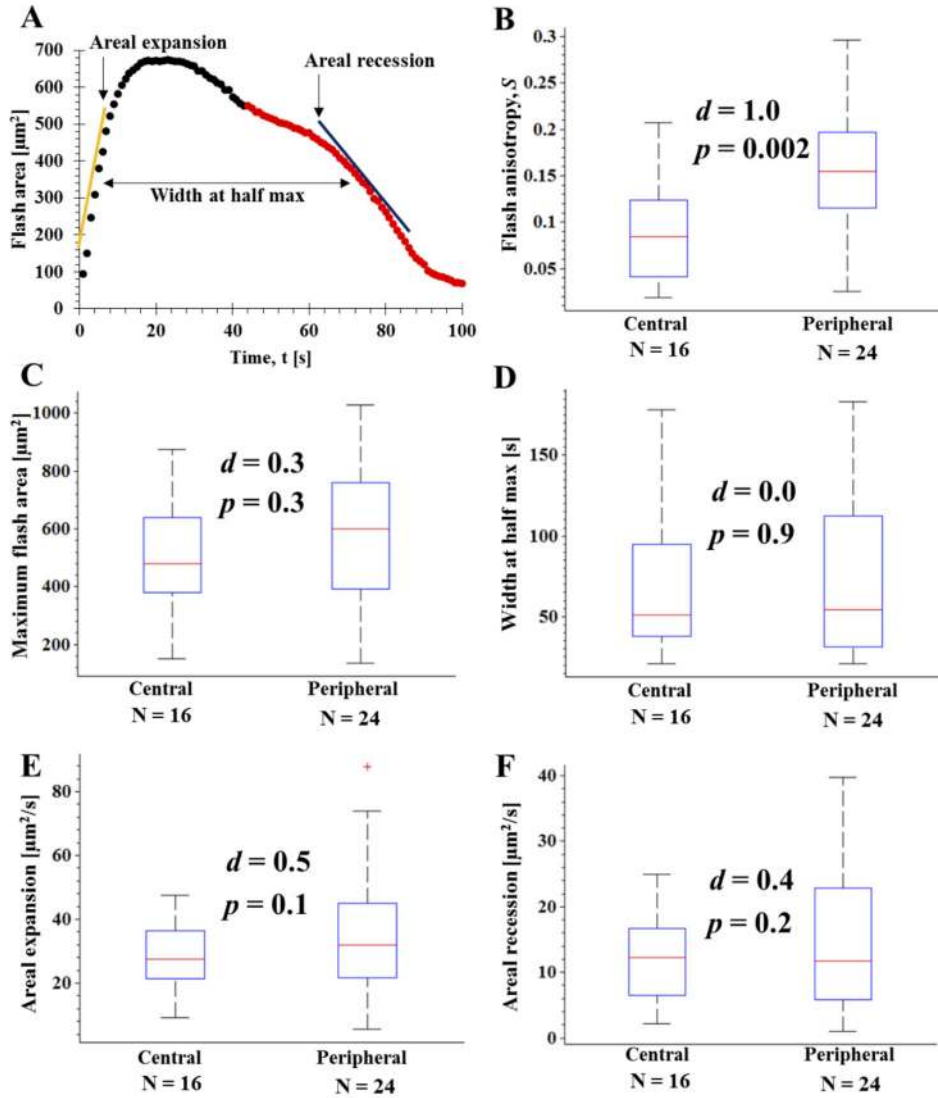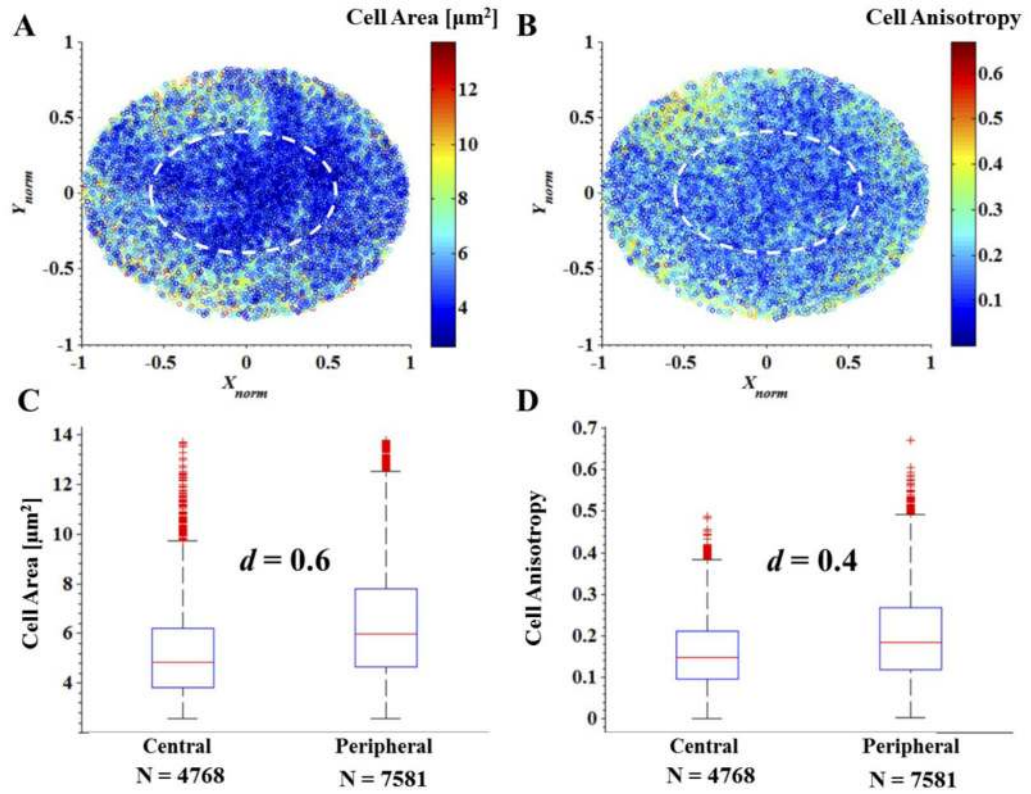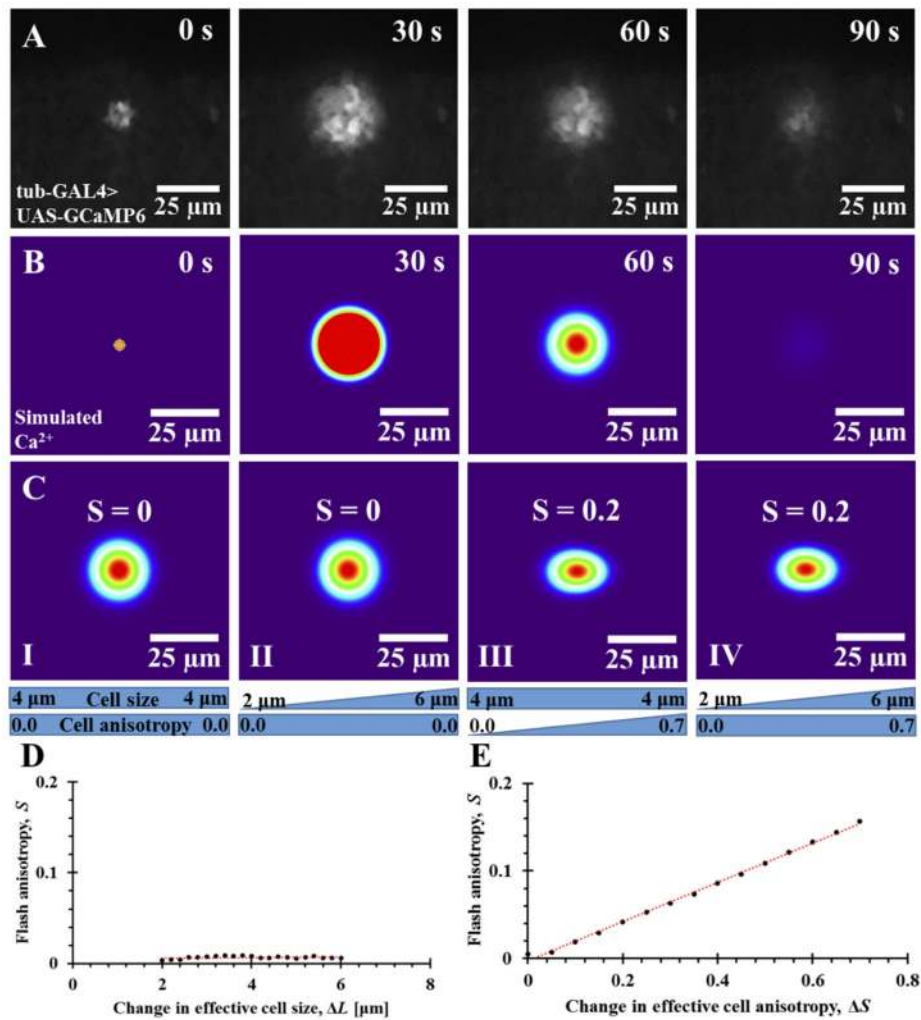
FIGURE 3.
(**A**) Characteristic plot of experimental flash area with time showing rapid initial parabolic propagation. The timescale for each flash is characterized by the full width at half maximum area. The propagation and recession of the flash is characterized by the slope of this curve at each half max point. We observe a distinct shift in the rate of change of flash area (red) during recession that is conserved in 36/40 flashes. (**B–F**) Quantification of intercellular Ca^{2+} flashes. Red lines represent median values of each category. The upper and lower ends of each box represent the quartiles at 25% and 75% probability respectively. Dashed lines indicate range of the data. Outliers are plotted as red crosses. Sample size for each category is listed below the bin. (**B**) Boxplot of flash anisotropy for laser induced flashes classed as being either central ($0.5 < z$) or peripheral ($0.5 \geq z$). Cohen's $d = 1.0$, indicating a large effective difference between the means. $p = 0.002$. (**C**) Boxplot of flash maximum area. Cohen's $d = 0.3$, indicating a small effective difference between the means. $p = 0.3$ (**D**) Boxplot of flash width at half max area. Cohen's $d = 0.0$, indicating negligible effective

difference between the means. $p = 0.9$. (**E**) Boxplot of flash areal expansion rate. Cohen's d $= 0.5$, indicating a moderate effective difference between the means. $p = 0.1$. (**F**) Boxplot of flash areal recession rate. Cohen's $d = 0.4$, indicating a small effective difference between the means. $p = 0.2$. All p-values from single factor ANOVA.
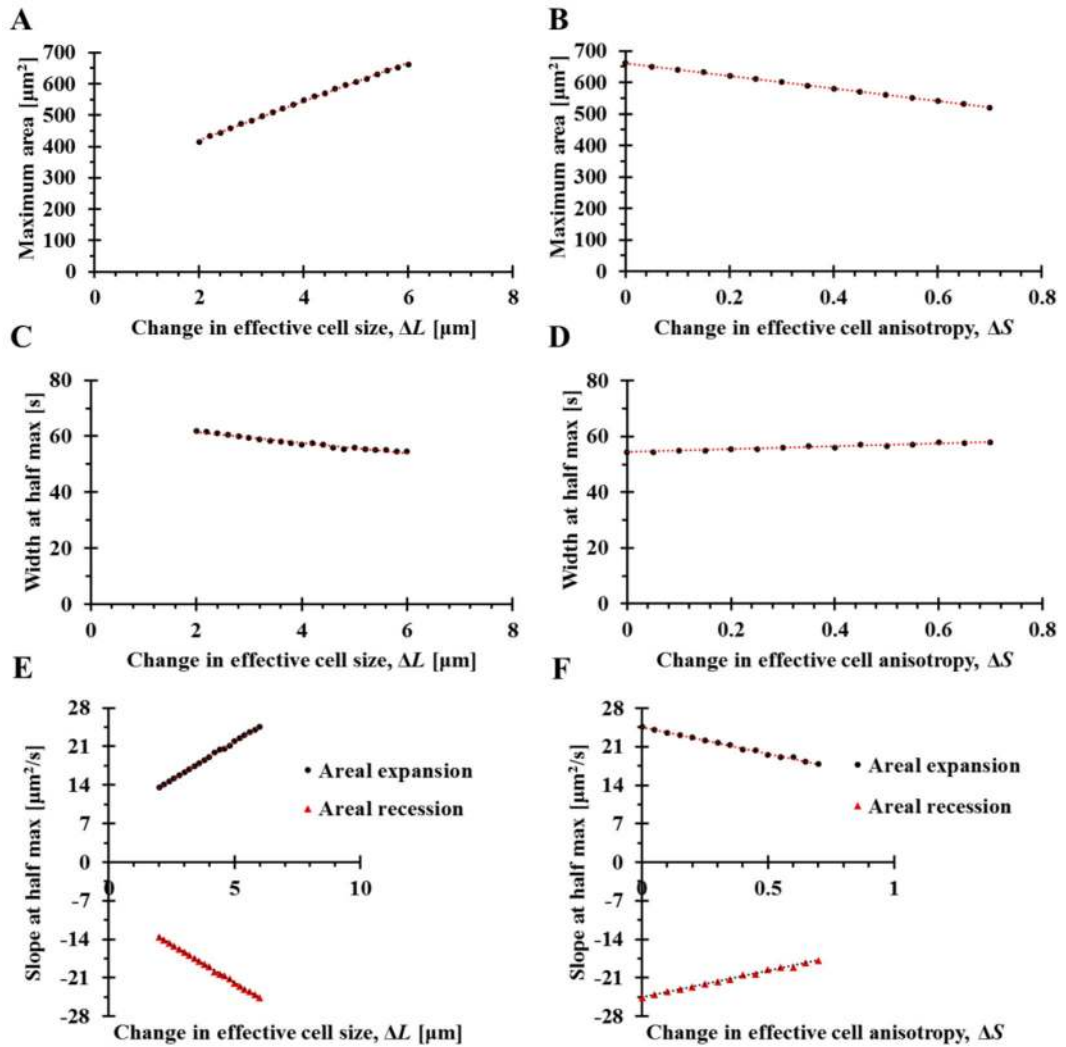
FIGURE 4.
(**A**) Color-coded point cloud of 12,349 cell areas from three, 3rd instar wing imaginal discs. Note the observable qualitative increase in cell area with increasing distance from pouch center along the radial PD axis. (**B**) Color-coded point cloud of cell fractional anisotropies from the same population of cells as in (**A**). Note the observable qualitative increase in cell anisotropy with increasing distance from pouch center. White ellipses in (**A**) and (**B**) show location of $z = 0.5$. (**C, D**) Boxplot analysis of cell morphology. Red lines represent median values of each category. The upper and lower ends of each box represent the quartiles at 25% and 75% probability respectively. Dashed lines indicate range of the data. Outliers are plotted as red crosses. Sample size for each category is listed below the bin. (**C**) Boxplot of cell area for cells classed as being either central ($0.5 < d$) or peripheral ($0.5 \geq d$). Cohen's d $= 0.6$, indicating a medium effective difference between the means. (**D**) Boxplot of cell anisotropy. Cohen's $d = 0.4$, indicating a small effective difference between the means.

FIGURE 5.
(A) Time-lapse montage of a typical experimentally observed flash from the disc periphery.
(B) Time-lapse montage of a simulated flash involving a gradient of both cell size (2 – 6 μm) and cell anisotropy (0.0 – 0.7). **(C)** The effect of spatially varying cell size and fractional anisotropy on simulated flash dynamics. The blue bars represent the imposed variation in cell size (upper) and fractional anisotropy (lower) across the spatial domain. A non-uniform distribution of cell size, or aspect ratio, leads to a spatially non-uniform, or anisotropic, effective diffusion coefficient for each diffusible species in the model. Frames shown are extracted at 60 s when asymmetry has reached its full extent. **(C, I)** Ca^{2+} flash with a uniform cell size (4 μm) and fractional anisotropy (S = 0). **(C, II)** Ca^{2+} flash with a gradient of cell size from 2–6 μm in the indicated direction and uniform fractional anisotropy. Propagation is still symmetric. **(C, III)** Ca^{2+} flash with uniform cell size and a gradient of fractional anisotropy from 0–0.7 in the indicated direction. Note that even with uniform cell sizes, an increase in fractional anisotropy leads to asymmetric propagation of the flash. **(C, IV)** Both a 2–6 μm cell size gradient and a 0–0.7 fractional anisotropy gradient are imposed on the sheet. There is no significant change to the asymmetry. **(D)** Graph of effective cell size gradients and their impact on flash anisotropy. Significant anisotropy does not develop

for physiologically relevant gradients of cell size. Note that although cell size may vary the characteristic length in both the x- and y- directions is equal when fractional anisotropy is zero. (**E**) Graph of effective cell anisotropy gradients and their impact on flash anisotropy. Anisotropy of the flash in these cases match the experimentally observed magnitude for physiologically observed gradients in cell anisotropy.

FIGURE 6.
The effects of cell size and cell anisotropy on flash morphology. (**A**) Plot of maximum flash area versus effective cell size from multiple *in silico* simulations. Effective size differences, ΔL and ΔS, represent linear variation across the computational domain starting at minimum value of 2 μm for cell size and 0 for anisotropy. For variable cell size simulations, imposed anisotropy is $S = 0$. For variable anisotropy simulations, imposed cell size is $L = 4$ μm. (**A**) The model predicts a linear increase in flash area with increasing cell size. (**B**) The model predicts a linear decrease in flash area with increasing cell anisotropy. (**C**) The model predicts a small linear decrease in flash timescale with increasing cell size (**D**) The model predicts a small linear increase in flash timescale with increasing cell anisotropy. (**E**) The model predicts a linear increase in both areal expansion (black circles) and areal recession (red triangles) rate with increasing cell size. (**E**) The model predicts a linear decrease in both areal expansion (black circles) and areal recession (red triangles) rate with increasing cell anisotropy. The opposing effects of cell size and cell anisotropy illustrated in (**A**)–(**F**)

explain the experimentally observed homogeneity in flash velocity, maximum area and timescale.

TABLE 1

Parameter values used in the computational model. Baseline values are taken from [35]. The values of k_{flux}, γ, k_P and the intercellular permeabilities were tuned to match the spatial extent and characteristic timescale of the experimentally observed flashes.

Parameter	Symbol	Value
Ca^{2+} flux when all IP$_3$ receptors are open and activated	k_{flux}	8 μM s^{-1}
Fraction of activated IP$_3$ receptors at zero Ca^{2+}	b	0.11
K$_m$ for activation of IP$_3$ receptors by Ca^{2+}	k_1	0.7 μM
K$_m$ for inactivation of IP$_3$ receptors by Ca^{2+}	k_2	0.7 μM
Time constant for inactivation of IP$_3$ receptors by Ca^{2+}	τ_h	0.2 s^{-1}
K$_m$ of ER Ca^{2+} pumps	k_γ	0.27 μM
Maximum pump rate for the ER pumps	γ	1.1 μM s^{-1}
Rate of Ca^{2+} leak from the ER	β	0.15 μM s^{-1}
K$_m$ for binding of IP$_3$ to its receptor	k_μ	0.01 μM
Maximal IP$_3$ degradation rate	V_P	0.08 s^{-1}
[IP$_3$] at which IP$_3$ degradation rate is half maximal	k_P	0.5 μM
Ca^{2+} diffusion coefficient	D_C^{intra}	20 μm^2 s^{-1}
IP$_3$ diffusion coefficient	D_P^{intra}	300 μm^2 s^{-1}
Intercellular permeability to IP$_3$	a_P	0.2 μm s^{-1}
Intercellular permeability to Ca	a_C	0.05 a_P
Length scale of individual cell (cell size)	l	2–6 μm
Fractional anisotropy of cell (cell elongation)	S	0 – 0.7
Length of tissue domain	L	80 μm